Enhancing Magnetic Light Emission with All-Dielectric Optical Nanoantennas

Maria Sanz-Paz[†], Cyrine Ernandes[‡,§], Juan Uriel Esparza[‡], Geoffrey W. Burr[#], Niek F. van Hulst[†,⊥], Agnès Maitre[‡], Lionel Aigouy[§], Thierry Gacoin[▽], Nicolas Bonod[‖], Maria F. Garcia-Parajo[†,⊥], Sébastien Bidault[°] and Mathieu Mivelle[†,‡]*

[†]ICFO - Institut de Ciencies Fotoniques, The Barcelona Institute of Science and Technology, Castelldefels, Barcelona, Spain

[‡]Sorbonne Université, CNRS, Institut des NanoSciences de Paris, UMR 7588, 75005 Paris, France

[§]Laboratoire de Physique et d'Etude des Matériaux, ESPCI Paristech, CNRS, 75005 Paris, France

[#]IBM Almaden Research Center, San Jose, California 95120, United States

[⊥]ICREA, Pg. Lluís Companys 23, 08010 Barcelona, Spain

[‖]Aix Marseille Univ, CNRS, Centrale Marseille, Institut Fresnel, Marseille, France

[▽]Laboratoire de Physique de la Matière Condensée, Ecole Polytechnique, Route de Saclay, 91128 Palaiseau, France

[°]ESPCI Paris, PSL Research University, CNRS, Institut Langevin, 75005 Paris, France

ABSTRACT. Electric and magnetic optical fields carry the same amount of energy. Nevertheless, the efficiency with which matter interacts with electric optical fields is commonly accepted to be at least 4 orders of magnitude higher than with magnetic optical fields. Here, we experimentally demonstrate that properly designed photonic nanoantennas can selectively manipulate the magnetic versus electric emission of luminescent nanocrystals. In particular, we show selective enhancement of magnetic emission from trivalent europium-doped nanoparticles in the vicinity of a nanoantenna tailored to exhibit a magnetic resonance. Specifically, by controlling the spatial coupling between emitters and an individual nanoresonator located at the edge of a near field optical scanning tip, we record with nanoscale precision local distributions of both magnetic and electric radiative local densities of states (LDOS). The map of the radiative LDOS reveals the modification of both the magnetic and electric quantum environments induced by the presence of the nanoantenna. This manipulation and enhancement of magnetic light-matter interaction by means of nanoantennas opens up new possibilities for the research fields of opto-electronics, chiral optics, nonlinear&nano-optics, spintronics and metamaterials, amongst others.

KEYWORDS: Dielectric and plasmonic nanoantennas, magnetic and electric LDOS, magnetic dipoles, magnetic light, near field optical microscopy.

TEXT. Landau postulated that the oscillation of light in the visible range was too fast to consider the influence of the optical magnetic field on the electrons,[1] justifying the magnetic permeability approximation $\mu(\omega) = \mu_0$ for macroscopic materials. Nevertheless, at the quantum level, the interaction between light and a quantum emitter is represented by a multipolar expansion of the interaction Hamiltonian:[2]

$$H_{int} = -p\cdot E(t) - m\cdot B(t) - [Q\nabla]\cdot E(t) - \ldots (1)$$

where p and m correspond to electric and magnetic dipoles, E and B to the electric and magnetic fields, and Q to the electric quadrupole. In here, if allowed by the selection rules, the term $p\cdot E(t)$ is orders of magnitude higher than any other term of equation 1, and this is why efforts have been made to mostly control, manipulate and enhance the emission of electric dipole sources. This has been achieved by means of interfaces,[3] cavities,[4] photonic crystals,[5]

and more recently by using plasmonic [6,7] and dielectric nanoantennas.[8-11] Although the electric interaction is significantly stronger than its magnetic counterpart, controlling the magnetic component of light-matter interactions remains little explored and could add a completely new degree of freedom in photonics and optoelectronics.

Recently, a series of experimental studies have demonstrated the detection [12-16] and manipulation of magnetic dipole transitions in lanthanide ions by means of metallic and dielectric interfaces in the visible range[17-20] and by plasmonic cavities in the near infrared.[21] In addition, in the past few years, theoretical studies have predicted the extraordinary properties of a certain class of photonic nanostructures,[22] in particular low loss dielectric resonators[23-35] and plasmonic nanoantennas,[36-39] to strongly enhance the optical magnetic field together with the spontaneous emission of magnetic dipoles,[26, 28, 31, 32, 35, 37, 39, 40] making them ideal to open new avenues in the emerging field of magneto-nanophotonics. Although several interesting studies have aimed at detecting and studying the magnetic component of light,[41-44] no experimental demonstration of the manipulation of magnetic spontaneous emission by means of nanoantennas has been reported so far at visible wavelengths. In here, we exploit the ability of photonic nanoantennas to interact with either the magnetic or the electric radiative local density of states (LDOS), to experimentally manipulate independently the magnetic and electric emission of luminescent emitters in the visible range. We demonstrate that coupling to a well-designed optical nanoantenna can increase either the magnetic or electric emission of trivalent europium doped nanoparticles, as predicted theoretically.[31, 35, 45] Finally, placing the nanoantenna at the extremity of an optical scanning tip provides full control over near-field interactions and the ability to record nanoscale maps of the relative electric and magnetic radiative LDOS (EMLDOS) around resonant nanostructures.

Manipulation of the emission of a nanoparticle containing magnetic dipolar (MD) and electric dipolar (ED) transitions in the near field, requires deterministic positioning of a well-defined magnetic or electric antenna in close proximity to the emitter. To this end, we combined top down focused-ion beam nanostructuring of a thin material (silicon and aluminum) and near-field scanning optical microscopy (NSOM) for control and manipulation at the nanoscale with nanometer precision. Here, two types of nanostructures are chosen: a magnetic cylindrical antenna (MCA) (Figure 1a) made of silicon and known to enhance the magnetic field[31, 33, 35] (Figure 1c), and an aluminum electric monopole antenna (EMA) (Figure 1b) to enhance the

electric field[46, 47] (Figure 1d)(See Figure S1 in Supporting Information for the corresponding electric and magnetic field intensities of each antenna). As sketched in Figure 1a,b, the presence of the optical nanoantenna in close proximity to a crystal containing MD and ED transitions (drawn as a purple particle) modifies the luminescence of the emitter by either enhancing the magnetic (green) or electric (red) emission. Experimentally, we use colloidal nanoparticles (50-70 nm in size) of YVO_4 doped with 20% Eu^{3+} (Figure S2 in Supporting Information). As shown in the partial band diagram of Figure 1e, trivalent europium ions feature MD ($^5D_0$ -> $^7F_1$, 590 nm) and ED ($^5D_0$ -> $^7F_2$, 610 nm) transitions (Figure 1f). Their emission spectrum can be therefore tailored by manipulating the EMLDOS with nanostructures. In this study, all other decay channels from $^5D_0$ to the ground state are considered as losses.

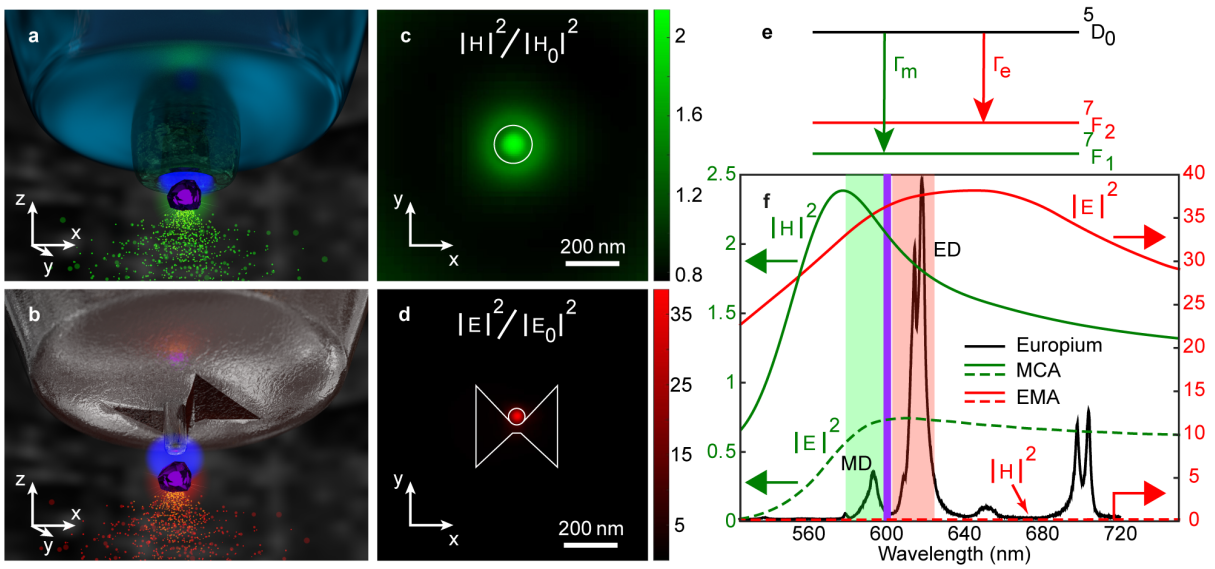

Figure 1. Principle of the experiment. Two types of photonic antennas are carved by a focused-ion beam (FIB) at the extremity of a near field tip. (a) A magnetic cylindrical antenna (MCA) made of silicon and (b) an electric monopole antenna (EMA) made of aluminum are brought in close proximity to a nanocrystal (purple particle) doped with trivalent europium ions featuring both magnetic and electric dipolar transitions. The magnetic emission is denoted in green color and the electric emission in red. (c) and (d) Numerical simulations of the normalized magnetic and electric field intensities in a transversal plane (xy) positioned 10 nm away from the MCA and the EMA respectively (calculated for a 590 nm excitation in the case of the MCA and 610 nm in the case of the EMA), the white circles represent the antennas contours. (e) Partial band diagram of Eu^{3+} describing the magnetic ($^5D_0$ -> $^7F_1$, green) and electric ($^5D_0$ -> $^7F_2$, red) dipolar transitions; Γ_m is the magnetic and Γ_e the electric radiative transition rates. (f) Theoretical magnetic and electric intensity spectral responses, normalized by their respective intensities in vacuum, of the MCA (green continuous and dashed curves) and the EMA (red continuous and dashed curves), calculated 10 nm below the centre of each antenna. The luminescence spectrum of the Eu^{3+} doped nanoparticle is displayed in black (see the Supporting Information for the particles synthesis). The purple line is the spectral position of the dichroic mirror that splits the magnetic and electric luminescence signals while the green and red bands represent the narrow bandpass filters used for each collection channel (see Figure S6 in the Supporting Information).

Antenna dimensions are set to feature a magnetic dipolar (MCA) and an electric monopolar (EMA) resonance in the visible range (Figure 1f and Figure S3 in the Supporting Information), and chosen to differentially cover two different parts of the spectrum so that each antenna mostly affects one transition: the magnetic resonance of the MCA is set to overlap with the MD transition and the electric resonance of the EMA with the ED transition of Eu^{3+} (black curve in Figure 1f). Although the resonances appear broad and overlap with both transitions, the magnetic resonance of the MCA will preferentially interact with the magnetic transition of europium and, likewise, for the electric resonance of the EMA.[26] Furthermore, Figure 1f provides the spectral evolution of electric and magnetic field intensities simulated 10 nm below the centre of the MCA and the EMA, respectively (dashed curves): both field intensities are actually inhibited with respect to vacuum (lower than 1) by the nanoantenna and should therefore inhibit electric and magnetic spontaneous emission, respectively, by reciprocity.[48]

Figure 2a,f display the scanning electron microscope (SEM) images of the MCA and EMA nanofabricated at the end of two different tapered optical fibers (See Figure S4 in the Supporting Information for a fabrication description). To reveal the ability of both nanostructures to manipulate the emission of the Eu^{3+} doped particle, we performed near field scans of 50-70 nm colloidal europium doped particles, deposited on a glass slide, with both types of antennas. The sample is excited at 465 nm, and the particle luminescence is collected through a high numerical aperture objective, with a dichroic mirror and a set of filters (See Figure S6 in the Supporting Information for technical details). This leads to the images displayed in Figure 2. Figure 2b-e correspond to the collected signal when the MCA is scanned over a single nanoparticle, while Figure 2g-j show the luminescence measured during the scan of the EMA over a few single particles and a cluster. Figure 2b,g depict the total intensity collected, while Figure 2c,h and Figure 2d,i respectively, provide the signal collected solely in the magnetic (590 nm) and electric (610 nm) channels. Note that these signals arise from the same excited state ($^5D_0$) and therefore are independent of the excitation channel (i.e. in near or far field), which happen at the transition $^7F_0 \rightarrow {}^5D_2$ of Eu^{3+}. As observed, the collected signals corresponding to electric and magnetic emission are significantly modified when coupling a MCA or EMA to the luminescent nanoparticles. In fact, while it is possible to distinguish emission in the case of the MCA in both electric and magnetic channels, in the case of the EMA, the luminescence intensity in the magnetic channel for single particles is negligible. Qualitatively, this can be better appreciated in Figure 2e,j where combined pictures

are obtained by normalizing the two channels with their respective maxima and by color-coding the magnetic signal in green and the electric one in red. The contrast is striking. In Figure 2e, corresponding to the MCA coupled to the particle, both magnetic and electrical signals are detected without spatial overlapping, implying that the maxima of the magnetic and electric radiative LDOS are spatially separated. In contrast, in the particles-EMA case (Figure 2j), the signal is clearly dominated by electric spontaneous emission.

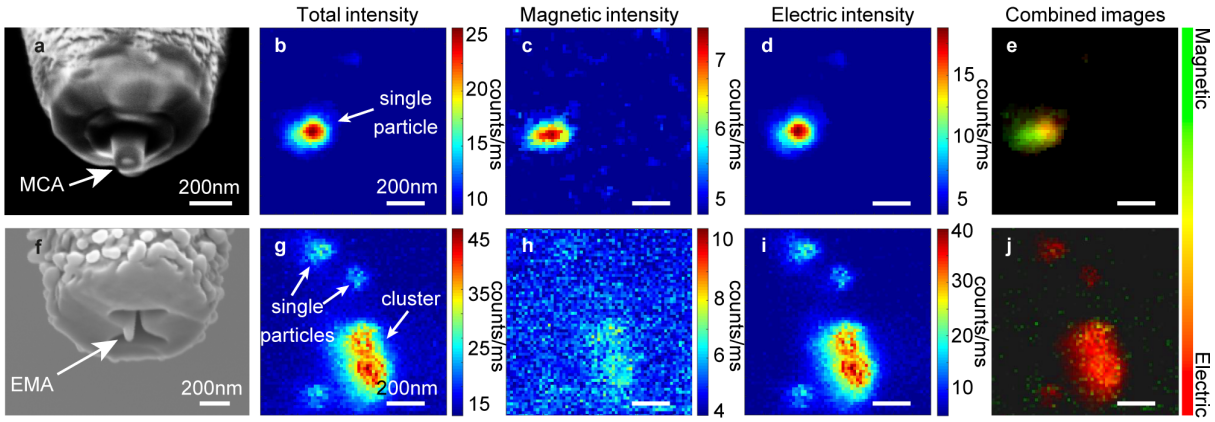

Figure 2. Near field coupling. SEM images of (a), the MCA and (f) the EMA, carved at the extremity of a near-field fibre probe. Luminescence intensity distributions monitored when scanning isolated Eu^{3+} doped nanoparticles in the near-field of a MCA (b-e), or an EMA (g-j): total collected intensity (b,g); collected magnetic emission (c,h); collected electric emission (d,i) and combined images (e,j) obtained by normalizing each detection channel to their maximum and color-coding the magnetic signal in green and the electric counterpart in red, before overlaying.

To quantitatively retrieve the influence of each nanoantenna on the magneto-electric emission of the nanocrystals, we introduce the branching ratios, which represent the relative weights of the two competing magnetic and electric transitions, and are defined by:[18]

$$\beta_m^{ant} = \frac{I_m^{lum}}{I_{total}^{lum}} = \frac{\Gamma_m}{\Gamma_m + \Gamma_e} \quad (2)$$

$$\beta_e^{ant} = 1 - \beta_m^{ant} = \frac{I_e^{lum}}{I_{total}^{lum}} = \frac{\Gamma_e}{\Gamma_m + \Gamma_e} \quad (3)$$

where I_m^{lum} and I_e^{lum} stand for the luminescence intensity collected either through the magnetic or electric channel after noise reduction, respectively, and I_{total}^{lum} is the total collected luminescence intensity.

Figure 3a,b display the spatial distributions of β_m^{ant} in the case of the MCA (Figure 3a, and Figure S7 for more examples) and β_e^{ant} in the case of the EMA (Figure 3b), calculated from Figure 2 (see Figure S8 in the Supporting Information for the corresponding electric (MCA) and magnetic (EMA) branching ratios). As expected from Figure 2, we observe two different trends: in the case of the MCA a clear gradient, going from a dominant magnetic to a dominant electric signal, is seen in the nanoscale variations of β_m^{ant}; while in the case of the EMA, a constant and essentially electric emission is collected. These trends demonstrate two major effects: first, the EMA is clearly an electric antenna favoring electric emission only. Second, the MCA has a dual property; it can strongly enhance the magnetic emission at given spatial positions, but it can also have an effect on the electric emission when the particle probes other spatial regions of the antenna.

To provide further insight on the nanoscale photonic properties of these resonators, Figure 3c and d provide experimental and theoretical line scans of β_m^{ant} and β_e^{ant} for each antenna (inset of Figure 3a,b and Figure S8 and 9 in the Supporting Information), demonstrating a relatively good agreement. From these line scans, we estimate a 2x average enhancement of the relative signal emanating from the MD transition when introducing the MCA and a 1.3x increase of the relative ED with the EMA with respect to the confocal case (i.e. without antennas, Figure S10 in the Supporting Information). These increases correspond to about 4x (MCA) and 80x (EMA) enhancements of respectively the magnetic (Γ_m/Γ_e) and electric (Γ_e/Γ_m) relative radiative decay rate (Figure S11 in the Supporting Information).

To further validate the ability of the MCA to enhance magnetic spontaneous emission and as a negative control, we performed a complementary experiment consisting in scanning in its near-field, and in the exact same conditions, fluorescent emitters that only feature electric dipolar transitions (Figure S12 in the Supporting Information). This complementary experiment demonstrates the unaffected behavior, by any other possible experimental bias, of the fluorescence emission when electric emitters are coupled to the MCA, confirming that the results observed in Figure 3a are due to nanoscale modifications of the magnetic LDOS.

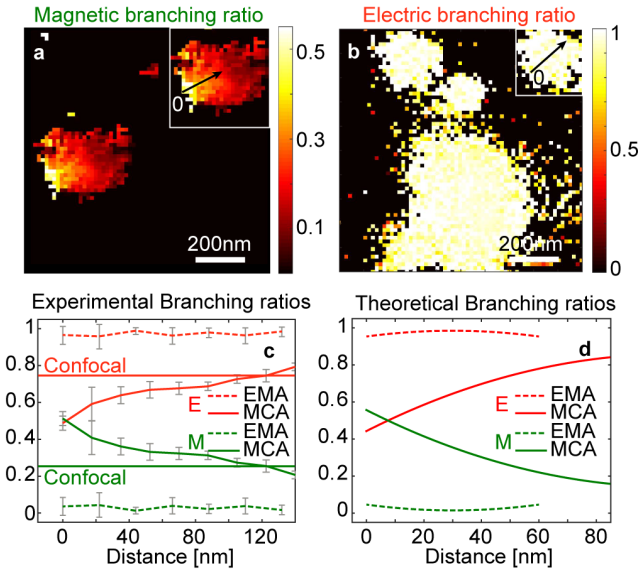

Figure 3. Magnetic and electric branching ratios. (a), Magnetic and (b) electric branching ratio distributions for the MCA and the EMA, respectively. In order to facilitate the visualization of these distributions, masks have been applied to render black all branching ratios corresponding to photoluminescence signals lower than 7.8 counts/ms in the case of the MCA (Figure 2b) and 9.2 counts/ms in the case of the EMA (Figure 2g); signals that would otherwise generate noise and would display unphysical values. (c) Experimental line scans of the branching ratios represented by the black lines seen in the insets in (a,b) and in Figure S8; in here, 0 represents the starting point and the arrow the direction of the scan. In (c) green corresponds to the magnetic branching ratio and red, to the electric branching ratios, the confocal constant lines represent the magnetic and electric relative signals detected without the presence of the antennas (Figure S10). The dashed and continuous lines stand for the EMA and MCA, respectively. The error bars represent the standard deviations. (d) Numerical counterpart of (c) where an isotropic MD and ED is scanned over a transverse plane along the MCA and the EMA at a distance of 10 nm below each antenna. For each position of the dipoles with respect to the nanoantennas, their radiative decay rates are calculated by integrating the full power emitted in far-field (see Figure S9 for more details on the procedure used for simulations).The slight discrepancy in distance between experiments and simulations is explained by the fact that numerical simulations consider a single isotropic point source, whereas the luminescent particles have typical dimensions ranging from 50 nm to 70 nm, convoluting the detected signal.

In addition, it should be mentioned that although the MCA antenna has a cylindrical symmetry, this symmetry is not observed in the branching ratio distributions displayed in Figure 3a. This is explained by a shape asymmetry of the fabricated antenna in the longitudinal direction, at final rim of the cylinder, as observed in Figure 2a: one side of the antenna is lower than the other inducing this asymmetry in the measured signal, as demonstrated below and described in Figure S13. As well, a possible tilt of the tip with respect to the sample during the experiment might increase this asymmetry.

Importantly, since both magnetic and electric transitions are related to the same excited state, the relative weight of each transition given by the branching ratios is directly related to the increase (or decrease) of the radiative magnetic and electric LDOS induced by the antenna:[18]

$$\beta_m^{ant} = \frac{\beta_m^{conf} \cdot \rho_m}{\beta_m^{conf} \cdot \rho_m + \beta_e^{conf} \cdot \rho_e} (4)$$

$$\beta_e^{ant} = 1 - \beta_m^{ant} (5)$$

where β_m^{conf}represents the magnetic and β_e^{conf} the electric branching ratios without the photonic antennas (i.e. far field excitation) (Figure 3c and Figure S10 in the Supporting Information), and ρ_m is the magnetic and ρ_e the electric radiative LDOS. Note that here, the strength of each magnetic and electric transition (their relative weight) is estimated to be equal to the branching ratios without the antennas (i.e. β_m^{conf} and β_e^{conf}).
From equations 4 and 5 we therefore introduce the relative radiative magnetic $\tilde{\rho}_m$ and electric $\tilde{\rho}_e$ LDOS[18] as:

$$\tilde{\rho}_m = \frac{\rho_m}{\rho_m + \rho_e} = \frac{\beta_e^{conf} \cdot \beta_m^{ant}}{\beta_e^{conf} \cdot \beta_m^{ant} + \beta_m^{conf} \cdot \beta_e^{ant}} (6)$$

and

$$\tilde{\rho}_e = 1 - \tilde{\rho}_m (7)$$

which represent the relative influence of the antennas on their electric and magnetic quantum environment. Figure 4a,b display the spatial distributions of $\tilde{\rho}_m$ and $\tilde{\rho}_e$ around the MCA. Although Figure 4a,b seem similar to Figure 3a and Figure S8, they actually hold extra information. Indeed, while β_m and β_e describe the relative strengths of two competing transitions, $\tilde{\rho}_m$ and $\tilde{\rho}_e$ quantify the effect of the environment on MD and ED transitions, at a given wavelength and independently of the emitter. Figure 4a,b are thus 2D maps of the

modification of the electric and magnetic quantum environment surrounding the silicon nanostructured antenna (see Figure S14 in the Supporting Information for the EMA case).

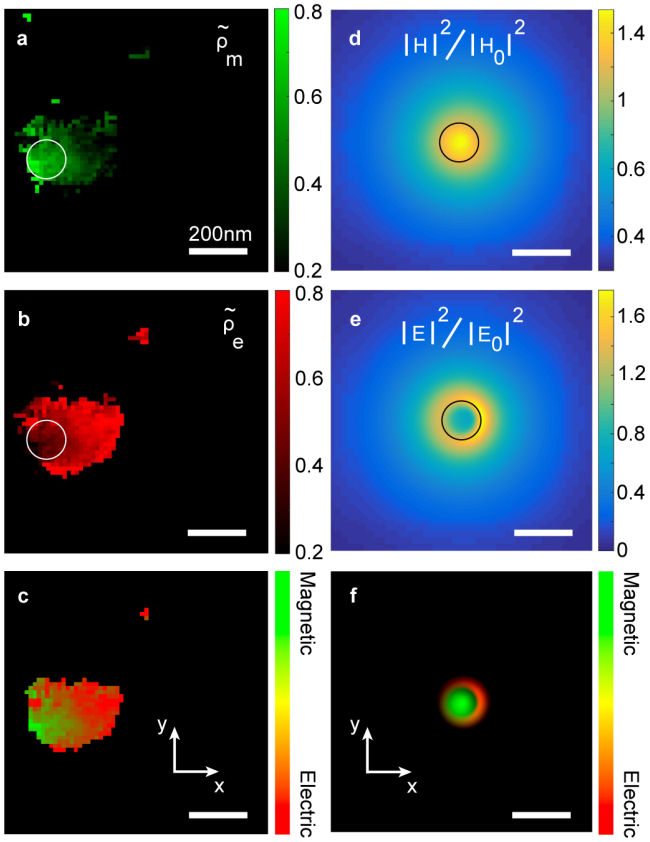

Figure 4. Relative radiative LDOS mapping. (a), magnetic and (b) electric relative radiative LDOS surrounding the MCA, (c) combined LDOS pictures from (a) and (b). In here, the same mask has been applied as in the case of Figure 3a. Normalized magnetic (d) and electric (e) field intensities in a transversal plane (xy) 20 nm below an asymmetric MCA (defined in Figure S13 of the Supporting Information). (f) Combined picture of (d) an e. The circles represent the outside rim of the MCA.

As mentioned above, the distribution of magnetic and electric relative radiative LDOS does not hold a cylindrical symmetric shape but instead features a gradient from preferentially magnetic to electric. To understand this behavior, numerical simulations were performed using an asymmetric MCA antenna (Figure S13 in the Supporting Information), based on the dimensions observed in the SEM image of Figure 2a. Figure 4d,e show plots of the

normalized theoretical magnetic (Figure 4d) and electric (Figure 4e) field intensities in a transversal plane positioned 20 nm away from the antenna. We clearly observe an asymmetric behavior of those intensities, which translates in a spatial displacement between electric and magnetic signals once computing a combined picture of those intensities (Figure 4f), in good qualitative agreement with the corresponding experimental combined image displayed in Figure 2e and Figure 4c. The remaining discrepancy is probably due to the convolution of the spatial magnetic and electric LDOS distributions by the non-spherical luminescent europium-doped nanoparticle that is scanned below the MCA. Moreover, the difference in sizes between the combined spots in Figure 4c and f can also be explained by the dimensions of the nanoparticles used experimentally (diameters typically ranging between 50 nm and 70 nm, Figure S2), which contributes to a convolution effect with the MCA that exhibits a slightly larger diameter (140 nm).

Finally, in order to fully express the influence of the antennas on their quantum environment in terms of the relative modification of the magnetic and electric LDOS, we define the degree of magnetic emission (DME) as:

$$\mathrm{DME} = \frac{\tilde{\rho}_m - \tilde{\rho}_e}{\tilde{\rho}_m + \tilde{\rho}_e} \quad (8)$$

Following equation 8, Figure 5a,b, display the 2D maps of DME for both antennas. Values of DME lower than 0 describe radiative electric LDOS enhancement (where electric emission is enhanced) and above 0, magnetic LDOS increase (where magnetic emission is increased). As expected, the DME in the case of the EMA is everywhere close to -1 (Figure 5b). Interestingly, a large area of about 90x120 nm^2 features an increase of magnetic emission for the case of the MCA, in good agreement with Figure 4f (See Figure S7d-f for more examples). To be more quantitative, Figure 5c,d respectively plot the distribution of DME for each pixel displayed in Figure 5a,b, when each antenna is scanning a single particle. We observe a broad distribution in the case of the MCA (Figure 5c), with in particular many antenna positions (number of pixels) giving a positive DME, and a very narrow distribution in the case of the EMA (Figure 5d), with only negative values and mainly shifted towards -1. These results unambiguously demonstrate an enhancement of magnetic spontaneous emission by means of a photonic nanoantenna (i.e. the MCA).

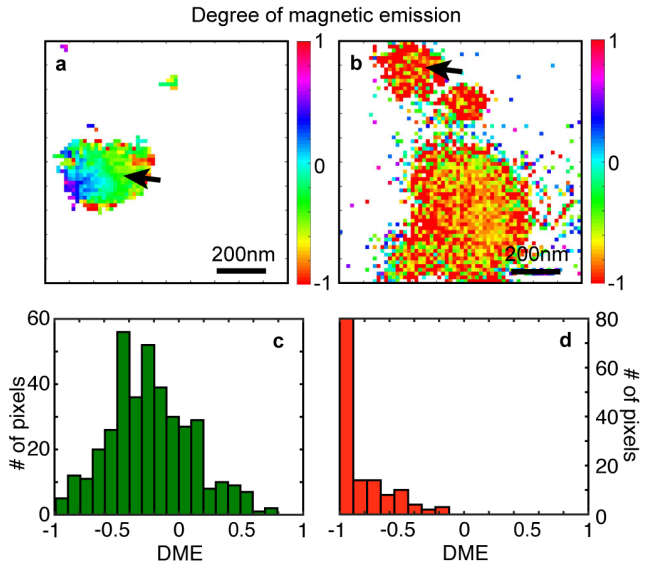

Figure 5. Degree of magnetic emission. DME 2D maps in the case of (a), the MCA and (b) the EMA. In here, the same masks have been applied as in the case of Figure 3a and b.(c) and (d) DME distribution obtained over every pixel of respectively (a) and (b)when a single particle is scanned by each antenna (indicated by an arrow), discarding noise pixels.

In summary, we experimentally demonstrated, for the first time, altogether manipulation, enhancement and control of the MD and ED transitions of quantum emitters using photonic nanoantennas, in good agreement with numerical simulations. First, manipulation by allowing the deterministic positioning of a Eu^{3+} doped nanoparticle in close proximity to the nanostructures. Second, average enhancement of respectively 2 and 1.3 times of the relative magnetic and electric emission intensities with respect to far field illumination altogether with respectively 4 and 80 times enhancement of magnetic (respectively, electric) over electric (respectively, magnetic) radiative decay rates and third, control by designing nanostructures featuring specifically magnetic or electric resonances. Furthermore, we mapped the spatial distributions of the magnetic and electric relative radiative LDOS surrounding these antennas and the degree of magnetic emission, allowing for a unique insight on how the nanostructures influence their environment at the optical quantum level.

These findings represent a turning point in light-matter interactions, by demonstrating that magnetic spontaneous emission can be dominant over its electric counterpart, thanks to optically resonant nanostructures. In particular, the boost of magnetic light and matter

interactions by magnetic nanoantennas opens new paradigms in various research fields involving magnetoelectric couplings such as spintronics, metamaterials, opto-electronics or chiral science. The latter, which is central in modern biochemistry and the evolution of life, would for instance directly benefit from this emerging research, as the magnetic component of light is crucial in light and chiral-matter interactions.[49-52]

ASSOCIATED CONTENT

Supporting Information.

Numerical simulations of the nanoantennas behavior. SEM image of the doped nanoparticles. Synthesis description of the particles. Nanoantennas fabrications. Scan of other particles. Far field experiments. Purely electric emitter experiment. Electric and magnetic counterparts of Figure 4a and b.

AUTHOR INFORMATION

Corresponding Author

*E-mail: mathieu.mivelle@insp.upmc.fr

Author Contributions

M.M., S.B., M.F.G-P., N.B., L.A, A.M., and N.F.vH. designed the research. M.M. designed, simulated and fabricated the antennas. G.B. developed the FDTD codes. T.G. synthesized the trivalent europium doped nanocrystals. M.S-P., C.E., J.E. and M.M. performed the measurements and analyzed the data. M.M., S.B. and N.B. wrote the manuscript with input from all authors.

The authors declare no competing financial interest.

ACKNOWLEDGMENT

M.M acknowledges support from the French "Investissements d'Avenir" program (Labex MATISSE), the DIM Nano-K program from "Région Ile de France", the CNRS emergence program and the ANR tremplin under reference ANR-17-ERC3-0006-01. M.F.G-P. and N.F.vH. acknowledge support from the EU-project NanoVista (FP7-ICT-2011-7, No 288263); the European Commission (ERC AdG 670949-LightNet); the Spanish Ministry of Economy and Competitiveness, through the "Severo Ochoa" program for Centres of Excellence in R&D (SEV-2015-0522), FIS2014-56107-R and FIS2015-69258-P; the Catalan Agència de Gestió d'Ajuts Universitaris i de Recerca (AGAUR; 2014SGR01540), Fundació Privada Cellex, Fundació Privada Mir-Puig, and Generalitat de Catalunya through the CERCA program. S.B. acknowledges support from LABEX WIFI (Laboratory of Excellence within the French Program "Investments for the Future") under references ANR-10-LABX-24 and ANR-10-IDEX-0001-02 PSL*.

REFERENCES

1. Landau, L. D.; Lífshíts, E. M.; Pitaevskii, L., *Electrodynamics of continuous media*. Pergamon press Oxford: 1984; Vol. 8.
2. Cowan, R. D., The theory of atomic structure and spectra. Univ of California Press: 1981; Vol. 3.
3. Chance, R.; Prock, A.; Silbey, R. *Adv. Chem. Phys* **1978,** 37, 65.
4. Vahala, K. J. *Nature* **2003,** 424, 839-846.
5. Lodahl, P.; Van Driel, A. F.; Nikolaev, I. S.; Irman, A.; Overgaag, K.; Vanmaekelbergh, D.; Vos, W. L. *Nature* **2004,** 430, 654-657.
6. Anger, P.; Bharadwaj, P.; Novotny, L. *Physical review letters* **2006,** 96, 113002.
7. Kühn, S.; Håkanson, U.; Rogobete, L.; Sandoghdar, V. *Physical review letters* **2006,** 97, 017402.
8. Caldarola, M.; Albella, P.; Cortés, E.; Rahmani, M.; Roschuk, T.; Grinblat, G.; Oulton, R. F.; Bragas, A. V.; Maier, S. A. *Nat. Commun.* **2015,** 6, 7915.
9. Staude, I.; Khardikov, V. V.; Fofang, N. T.; Liu, S.; Decker, M.; Neshev, D. N.; Luk, T. S.; Brener, I.; Kivshar, Y. S. *ACS Photonics* **2015,** 2, 172-177.
10. Bouchet, D.; Mivelle, M.; Proust, J.; Gallas, B.; Ozerov, I.; Garcia-Parajo, M. F.; Gulinatti, A.; Rech, I.; De Wilde, Y.; Bonod, N. *Physical Review Applied* **2016,** 6, 064016.

11. Regmi, R.; Berthelot, J.; Winkler, P. M.; Mivelle, M.; Proust, J.; Bedu, F. d. r.; Ozerov, I.; Begou, T.; Lumeau, J.; Rigneault, H. *Nano Letters* **2016,** 16, 5143-5151.
12. Karaveli, S.; Zia, R. *Physical review letters* **2011,** 106, 193004.
13. Taminiau, T. H.; Karaveli, S.; van Hulst, N. F.; Zia, R. *Nature communications* **2012,** 3, 979.
14. Karaveli, S.; Weinstein, A. J.; Zia, R. *Nano Lett.* **2013,** 13, 2264-2269.
15. Cueff, S.; Li, D.; Zhou, Y.; Wong, F. J.; Kurvits, J. A.; Ramanathan, S.; Zia, R. *Nat. Commun.* **2015,** 6, 8636.
16. Kasperczyk, M.; Person, S.; Ananias, D.; Carlos, L. D.; Novotny, L. *Physical review letters* **2015,** 114, 163903.
17. Noginova, N.; Barnakov, Y.; Li, H.; Noginov, M. *Optics express* **2009,** 17, 10767-10772.
18. Aigouy, L.; Cazé, A.; Gredin, P.; Mortier, M.; Carminati, R. *Physical review letters* **2014,** 113, 076101.
19. Hussain, R.; Kruk, S. S.; Bonner, C. E.; Noginov, M. A.; Staude, I.; Kivshar, Y. S.; Noginova, N.; Neshev, D. N. *Optics letters* **2015,** 40, 1659-1662.
20. Rabouw, F. T.; Prins, P. T.; Norris, D. J. *Nano Letters* **2016,** 16, 7254-7260.
21. Choi, B.; Iwanaga, M.; Sugimoto, Y.; Sakoda, K.; Miyazaki, H. T. *Nano Letters* **2016,** 16, 5191-5196.
22. Baranov, D. G.; Savelev, R. S.; Li, S. V.; Krasnok, A. E.; Alù, A. *Laser & Photonics Reviews* **2017,** 11, 1600268.
23. Evlyukhin, A. B.; Reinhardt, C.; Seidel, A.; Luk'yanchuk, B. S.; Chichkov, B. N. *Phys. Rev. B* **2010,** 82, 045404.
24. García-Etxarri, A.; Gómez-Medina, R.; Froufe-Pérez, L. S.; López, C.; Chantada, L.; Scheffold, F.; Aizpurua, J.; Nieto-Vesperinas, M.; Sáenz, J. *Opt. Express* **2011,** 19, 4815-4826.
25. Evlyukhin, A. B.; Novikov, S. M.; Zywietz, U.; Eriksen, R. L.; Reinhardt, C.; Bozhevolnyi, S. I.; Chichkov, B. N. *Nano Lett.* **2012,** 12, 3749-3755.
26. Rolly, B.; Bebey, B.; Bidault, S.; Stout, B.; Bonod, N. *Physical Review B* **2012,** 85, 245432.
27. Schmidt, M. K.; Esteban, R.; Sáenz, J.; Suárez-Lacalle, I.; Mackowski, S.; Aizpurua, J. *Opt. Express* **2012,** 20, 13636-13650.
28. Albella, P.; Poyli, M. A.; Schmidt, M. K.; Maier, S. A.; Moreno, F.; Sáenz, J. J.; Aizpurua, J. *The Journal of Physical Chemistry C* **2013,** 117, 13573-13584.
29. Coenen, T.; Van De Groep, J.; Polman, A. *ACS Nano* **2013,** 7, 1689-1698.
30. Zambrana-Puyalto, X.; Bonod, N. *Phys. Rev. B* **2015,** 91, 195422.
31. Feng, T.; Xu, Y.; Liang, Z.; Zhang, W. *Opt. Lett.* **2016,** 41, 5011-5014.
32. Kuznetsov, A. I.; Miroshnichenko, A. E.; Brongersma, M. L.; Kivshar, Y. S.; Luk'yanchuk, B. *Science* **2016,** 354, aag2472.
33. van de Haar, M. A.; van de Groep, J.; Brenny, B. J.; Polman, A. *Optics express* **2016,** 24, 2047-2064.
34. Cihan, A. F.; Curto, A. G.; Raza, S.; Kik, P. G.; Brongersma, M. L. *arXiv preprint arXiv:1709.04999* **2017**.
35. Li, J.; Verellen, N.; Van Dorpe, P. *ACS Photonics* **2017**.
36. Grosjean, T.; Mivelle, M.; Baida, F.; Burr, G.; Fischer, U. *Nano letters* **2011,** 11, 1009-1013.
37. Hein, S. M.; Giessen, H. *Physical review letters* **2013,** 111, 026803.

38. Chigrin, D. N.; Kumar, D.; Cuma, D.; von Plessen, G. *ACS Photonics* **2015,** 3, 27-34.
39. Mivelle, M.; Grosjean, T.; Burr, G. W.; Fischer, U. C.; Garcia-Parajo, M. F. *ACS Photonics* **2015,** 2, 1071-1076.
40. Baranov, D. G.; Savelev, R. S.; Li, S. V.; Krasnok, A. E.; Alù, A. *Laser & Photonics Reviews* **2017**.
41. Devaux, E.; Dereux, A.; Bourillot, E.; Weeber, J.-C.; Lacroute, Y.; Goudonnet, J.-P.; Girard, C. *Phys. Rev. B* **2000,** 62, 10504.
42. Kihm, H.; Koo, S.; Kim, Q.; Bao, K.; Kihm, J.; Bak, W.; Eah, S.; Lienau, C.; Kim, H.; Nordlander, P. *Nat. Commun.* **2011,** 2, 451.
43. Denkova, D.; Verellen, N.; Silhanek, A. V.; Valev, V. K.; Dorpe, P. V.; Moshchalkov, V. V. *ACS Nano* **2013,** 7, 3168-3176.
44. Caselli, N.; La China, F.; Bao, W.; Riboli, F.; Gerardino, A.; Li, L.; Linfield, E. H.; Pagliano, F.; Fiore, A.; Schuck, P. J. *Scientific reports* **2015,** 5.
45. Feng, T.; Zhang, W.; Liang, Z.; Xu, Y.; Miroshnichenko, A. E. *ACS Photonics* **2017**.
46. Taminiau, T.; Stefani, F.; Segerink, F.; Van Hulst, N. *Nature Photonics* **2008,** 2, 234-237.
47. Mivelle, M.; van Zanten, T. S.; Garcia-Parajo, M. F. *Nano letters* **2014,** 14, 4895-4900.
48. Novotny, L.; Hecht, B., *Principles of nano-optics*. Cambridge university press: 2012.
49. Tang, Y.; Cohen, A. E. *Phys. Rev. Lett.* **2010,** 104, 163901.
50. Klimov, V. V.; Guzatov, D. V.; Ducloy, M. *EPL (Europhysics Letters)* **2012,** 97, 47004.
51. Ho, C.-S.; Garcia-Etxarri, A.; Zhao, Y.; Dionne, J. *ACS Photonics* **2017,** 4, 197-203.
52. Valev, V. K.; Govorov, A. O.; Pendry, J. *Advanced Optical Materials* **2017,** 5.

TABLE OF CONTENTS GRAPHIC

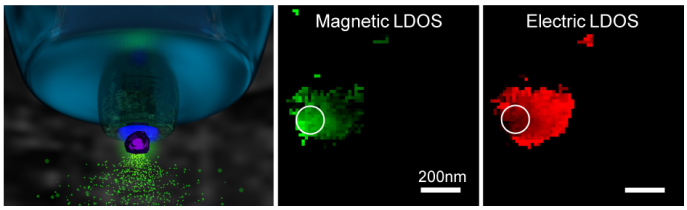

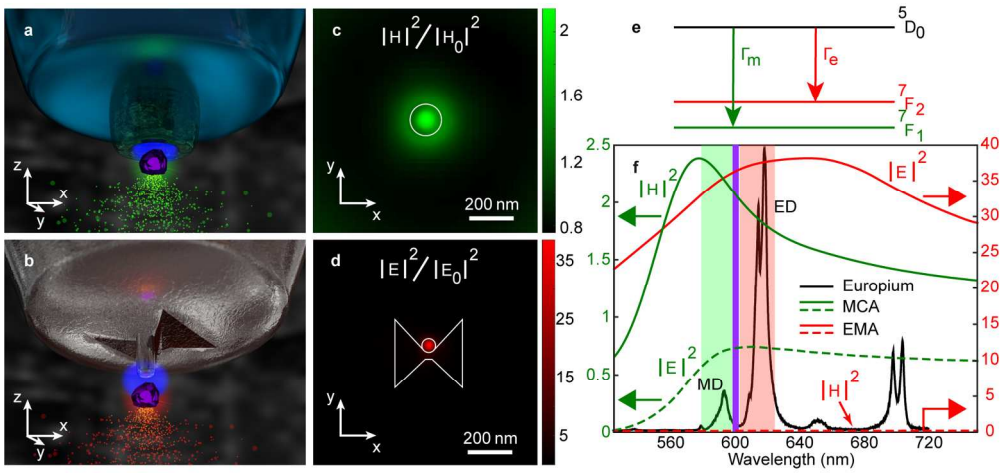

Figure 1. Principle of the experiment. Two types of photonic antennas are carved by a focused-ion beam (FIB) at the extremity of a near field tip. (a) A magnetic cylindrical antenna (MCA) made of silicon and (b) an electric monopole antenna (EMA) made of aluminum are brought in close proximity to a nanocrystal (purple particle) doped with trivalent europium ions featuring both magnetic and electric dipolar transitions. The magnetic emission is denoted in green color and the electric emission in red. (c) and (d) Numerical simulations of the normalized magnetic and electric field intensities in a transversal plane (xy) positioned 10 nm away from the MCA and the EMA respectively (calculated for a 590 nm excitation in the case of the MCA and 610 nm in the case of the EMA), the white circles represent the antennas contours. (e) Partial band diagram of Eu3+ describing the magnetic (5D0 -> 7F1, green) and electric (5D0 -> 7F2, red) dipolar transitions; Γm is the magnetic and Γe the electric radiative transition rates. (f) Theoretical magnetic and electric intensity spectral responses, normalized by their respective intensities in vacuum, of the MCA (green continuous and dashed curves) and the EMA (red continuous and dashed curves), calculated 10 nm below the centre of each antenna. The luminescence spectrum of the Eu3+ doped nanoparticle is displayed in black (see the Supporting Information for the particles synthesis). The purple line is the spectral position of the dichroic mirror that splits the magnetic and electric luminescence signals while the green and red bands represent the narrow bandpass filters used for each collection channel (see Figure S6 in the Supporting Information).

168x79mm (300 x 300 DPI)

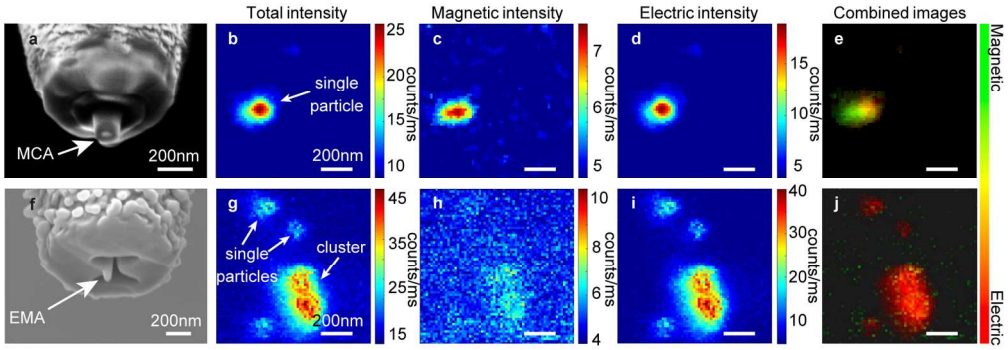

Figure 2. Near field coupling. SEM images of (a), the MCA and (f) the EMA, carved at the extremity of a near-field fibre probe. Luminescence intensity distributions monitored when scanning isolated Eu3+ doped nanoparticles in the near-field of a MCA (b-e), or an EMA (g-j): total collected intensity (b,g); collected magnetic emission (c,h); collected electric emission (d,i) and combined images (e,j) obtained by normalizing each detection channel to their maximum and color-coding the magnetic signal in green and the electric counterpart in red, before overlaying.

169x59mm (300 x 300 DPI)

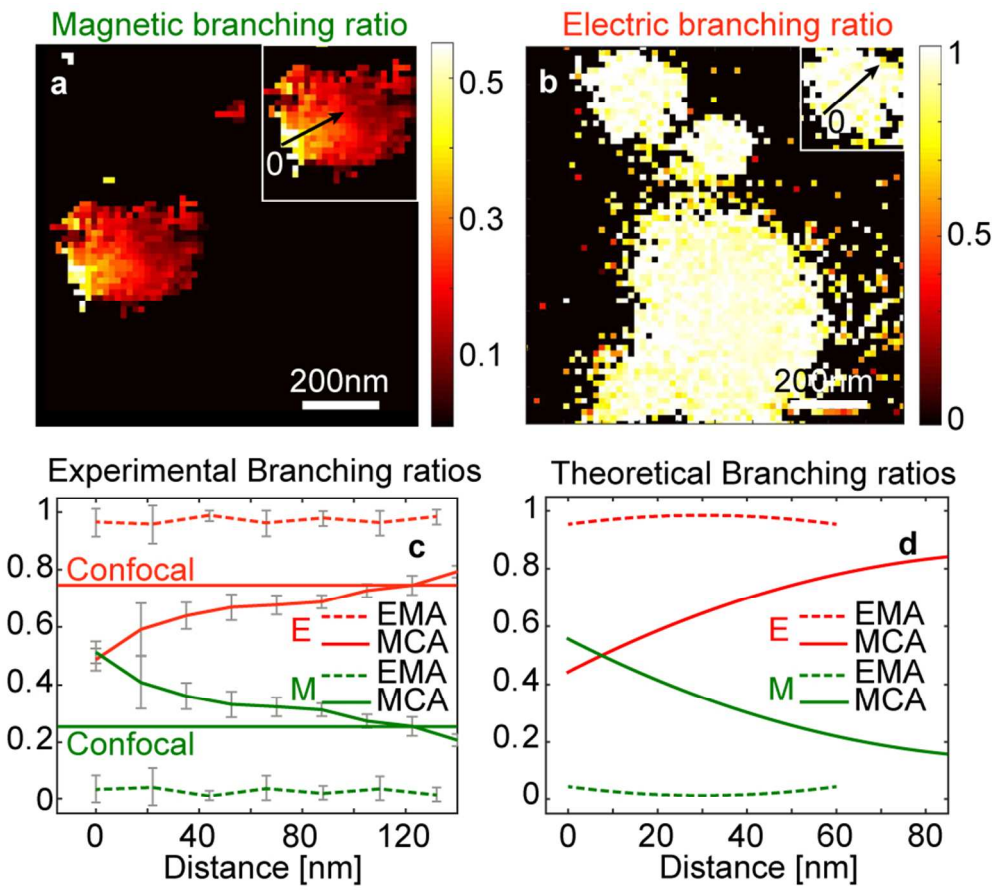

Figure 3. Magnetic and electric branching ratios. (a), Magnetic and (b) electric branching ratio distributions for the MCA and the EMA, respectively. In order to facilitate the visualization of these distributions, masks have been applied to render black all branching ratios corresponding to photoluminescence signals lower than 7.8 counts/ms in the case of the MCA (Figure 2b) and 9.2 counts/ms in the case of the EMA (Figure 2g); signals that would otherwise generate noise and would display unphysical values. (c) Experimental line scans of the branching ratios represented by the black lines seen in the insets in (a,b) and in Figure S8; in here, 0 represents the starting point and the arrow the direction of the scan. In (c) green corresponds to the magnetic branching ratio and red, to the electric branching ratios, the confocal constant lines represent the magnetic and electric relative signals detected without the presence of the antennas (Figure S10). The dashed and continuous lines stand for the EMA and MCA, respectively. The error bars represent the standard deviations. (d) Numerical counterpart of (c) where an isotropic MD and ED is scanned over a transverse plane along the MCA and the EMA at a distance of 10 nm below each antenna. For each position of the dipoles with respect to the nanoantennas, their radiative decay rates are calculated by integrating the full power emitted in far-field (see Figure S9 for more details on the procedure used for simulations).The slight discrepancy in distance between experiments and simulations is explained by the fact that numerical simulations consider a single isotropic point source, whereas the luminescent particles have typical dimensions ranging from 50 nm to 70 nm, convoluting the detected signal.

86x77mm (300 x 300 DPI)

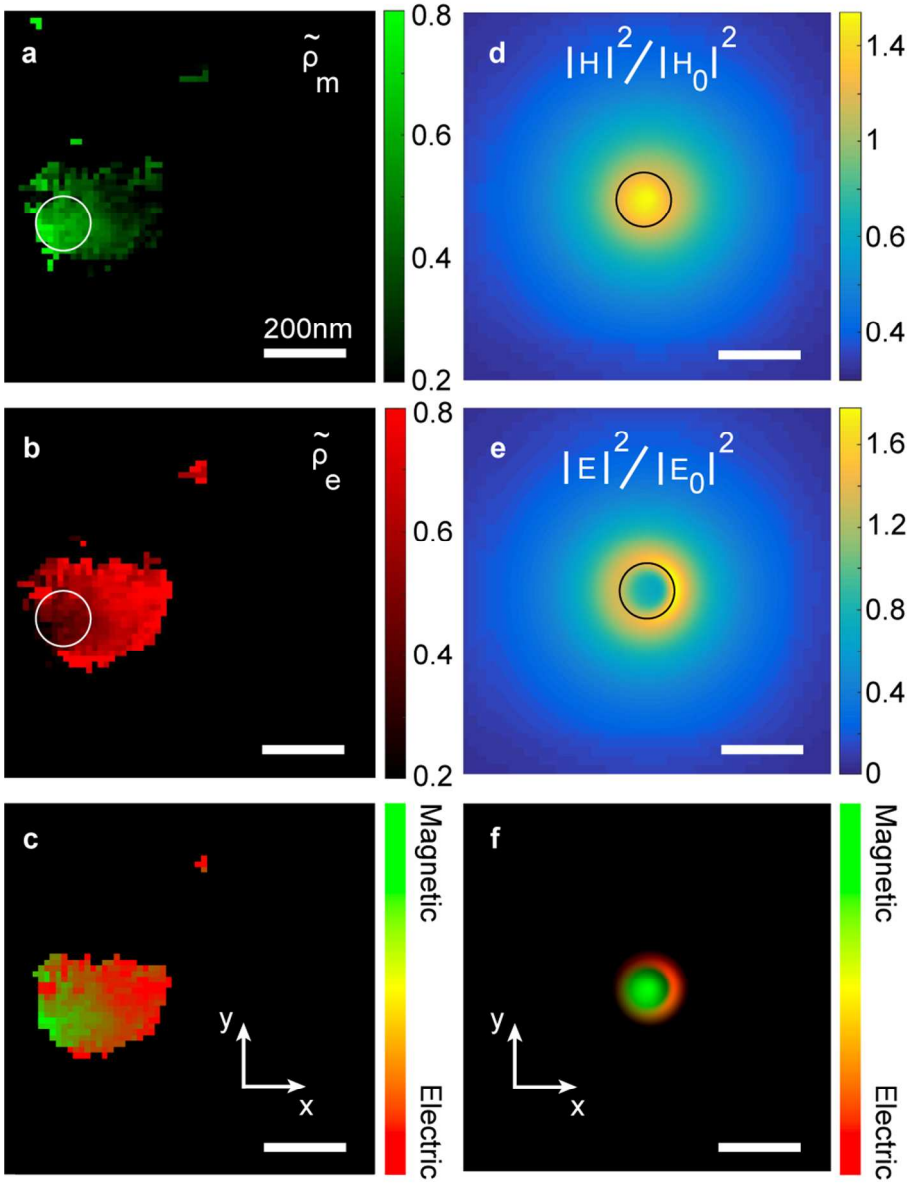

Figure 4. Relative radiative LDOS mapping. (a), magnetic and (b) electric relative radiative LDOS surrounding the MCA, (c) combined LDOS pictures from (a) and (b). In here, the same mask has been applied as in the case of Figure 3a. Normalized magnetic (d) and electric (e) field intensities in a transversal plane (xy) 20 nm below an asymmetric MCA (defined in Figure S13 of the Supporting Information). (f) Combined picture of (d) an e. The circles represent the outside rim of the MCA.

87x115mm (300 x 300 DPI)

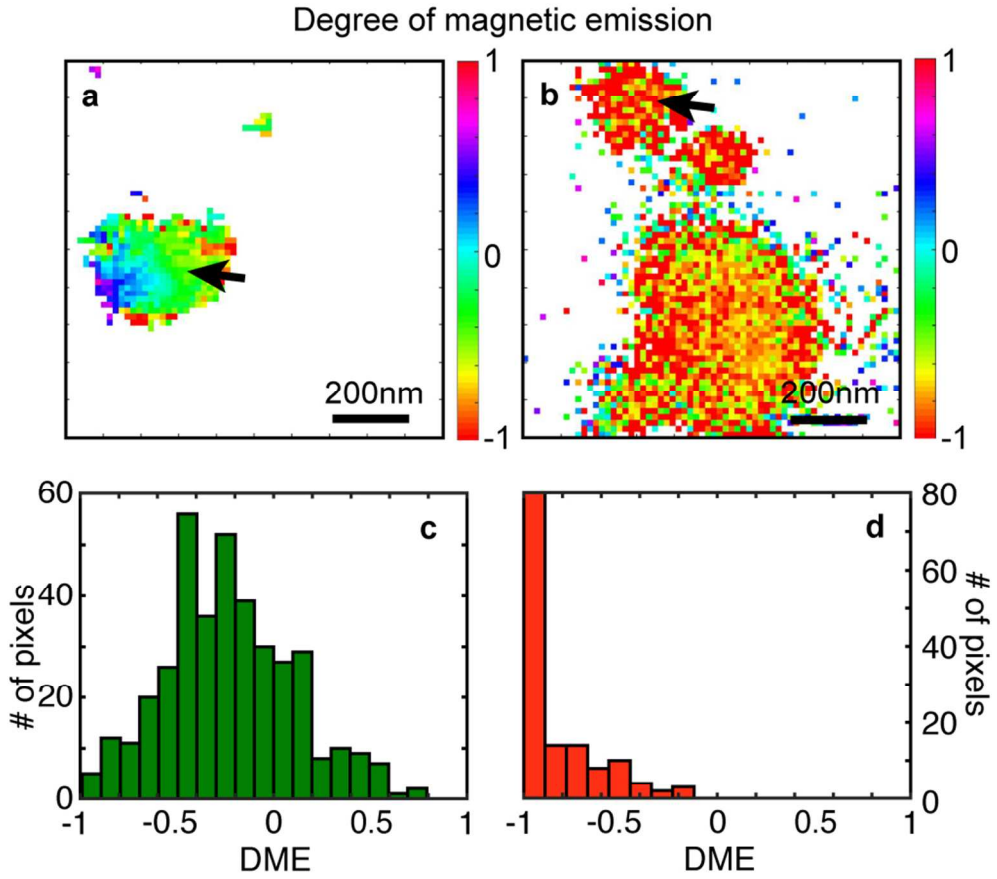

Figure 5. Degree of magnetic emission. DME 2D maps in the case of (a), the MCA and (b) the EMA. In here, the same masks have been applied as in the case of Figure 3a and b.(c) and (d) DME distribution obtained over every pixel of respectively (a) and (b)when a single particle is scanned by each antenna (indicated by an arrow), discarding noise pixels.

87x76mm (300 x 300 DPI)

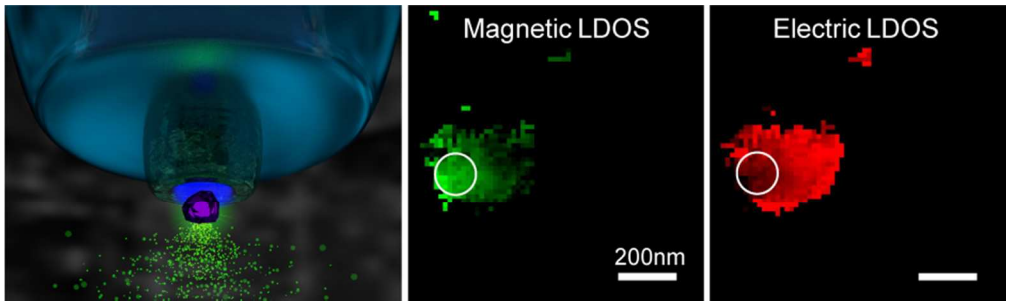

TABLE OF CONTENTS GRAPHIC

79x23mm (300 x 300 DPI)